



Reactive-convective dissolution in a porous medium: the storage of carbon dioxide in saline aquifers

Parama Ghoshal^{a,b}, Min Chan Kim^c and Silvana S.S. Cardoso^{a*}

Received 00th January 20xx,
Accepted 00th January 20xx

DOI: 10.1039/x0xx00000x

www.rsc.org/

We quantify the destabilising effect of a first-order chemical reaction on the fingering instability of a diffusive boundary layer in a porous medium. Using scaling, we show that the dynamics of such a reactive boundary layer is fully determined by two dimensionless groups: Da/Ra^2 , which measures the timescale for convection compared to those for reaction and diffusion; and β_C/β_A , which reflects the density change induced by the product relative to that of the diffusing solute. Linear stability and numerical results for β_C/β_A in the range 0 – 10 and Da/Ra^2 in the range 0-0.01 are presented. It is shown that the chemical reaction increases the growth rate of a transverse perturbation and favours large wavenumbers compared to the inert system. Higher β_C/β_A and Da/Ra^2 not only accelerate the onset of convection, but crucially also double the transport of the solute compared to the inert system. Application of our findings to the storage of carbon dioxide in carbonate saline aquifers reveals that chemical equilibrium curtails this increase of CO₂ flux to 50%.

1 Introduction

Dissolution driven convection in porous media has received recent interest in context of the long-term geological storage of carbon dioxide in underground, natural, brine filled caverns, often referred to as saline aquifers.¹⁻⁴ Following injection into the saline aquifer, dissolution of supercritical carbon dioxide in the host brine causes a local density increase leading to gravitational instability of the diffusive boundary layer and formation of convective fingers. Convection enhances further carbon-dioxide dissolution in the brine.⁵⁻⁷ Such dissolution-driven Rayleigh-Darcy convection has been extensively studied in inert systems, both theoretically^{3,5,7,8-16} and experimentally.^{6,17-20}

Chemical reaction of the dissolved carbon dioxide with the underground host rock can lead to long-term sequestration. However, the geochemistry can severely complicate the situation by interacting with the fluid motion, altering the hydrodynamic instability and the spatio-temporal convection patterns.²¹⁻²² Previous works on reactive systems have demonstrated stabilizing effects of chemical reaction in the case of the removal of solute from the system.^{21,22-26} It has been shown that formation of a solid product can stabilize the diffusive boundary layer, resulting in a delay in the time for onset of convection and a severe reduction of the convective motion. As a result, the lower part of the reservoir may remain

unutilised.^{22,27-33}

The effect of chemical reaction on Rayleigh-Darcy convection when the reaction product contributes to the density field has been only partially explored. Previous works³⁴⁻³⁶ have identified configurations with destabilizing effects of second-order chemical reactions, using linear stability analysis and laboratory experiments. The nonlinear behaviour has only very recently been touched upon experimentally.^{37,38} The effects of variation in density contrast between the diffusing solute and the reaction product on the complex nonlinear dynamic behaviour of the boundary layer, viz., spatio-temporal concentration profile of the solute and the product and the convective-reactive solute dissolution flux remain unexplored. Moreover, there is substantial scope for theoretical characterization of the nonlinear dynamics of the reactive boundary layer and the dynamic evolution and interaction of the finger patterns along with their sensitivity to the reaction kinetics and the density change induced by the reaction. Additionally, the effects of a first-order chemical reaction on the stability of a boundary layer, when the product contributes to the density field, remain largely unexplored. In this paper, we address all the above gaps in knowledge on reactive boundary layers in porous media. We present a linear stability analysis coupled with numerical simulations, to investigate the stability and the nonlinear dynamics of a diffusive boundary layer undergoing a first-order chemical reaction where the product remains in the liquid phase and induces a density change of the fluid mixture. The effects of reaction on the time for onset of convection and on the intensity of the convective motion are presented. The growth and complex non-linear behaviour of the boundary layer is quantitatively characterized by the spatio-temporal concentration profiles of the reactant and product, along with

^a Department of Chemical Engineering and Biotechnology, University of Cambridge, Cambridge CB2 3RA, Cambridge, United Kingdom.

^b Department of Chemical Engineering, Jadavpur University, Kolkata-700032, India.

^c Department of Chemical Engineering, Jeju National University, Jeju-63243, Republic of Korea.

*Corresponding author, Email: sssc1@cam.ac.uk.

their sensitivity to the governing parameters. We quantify the accelerated dissolution flux driven by the reaction. The effects of chemical reaction on the formation and interaction of convective fingers are also quantified.

Our findings are of relevance in the geo-storage of carbon dioxide. An example of application is the qualitative and quantitative prediction of convection phenomena in carbonate saline reservoirs, which we discuss in section 4.

2 Model

2.1 Governing Equations

We consider the transport of a solute A as it dissolves at the top of a fluid-saturated porous medium [Fig. 1]. The porous medium is two dimensional, homogeneous, and isotropic. The solute A irreversibly undergoes a first-order chemical reaction with chemical species B present in the host porous rock, resulting in product C that remains in solution: $A(aq) + B(s) \rightarrow C(aq)$. Both the solute A and the product C contribute to the density of the solution. The solute and the product are advected by the fluid as it moves in the pore space. We assume incompressible, Darcy flow under Boussinesq conditions, so that

$$\nabla \cdot \mathbf{v} = 0, \quad (1)$$

$$\mathbf{v} = -\frac{k_p}{\mu} (\nabla p - \rho_r \beta_A C_A \mathbf{j} - \rho_r \beta_C C_C \mathbf{j}). \quad (2)$$

Here, $\mathbf{v} = (u, v)$ is the Darcy velocity vector, $p = P - \rho_r g z$ is the reduced pressure field, obtained by eliminating hydrostatic pressure from the local pressure P , g is the acceleration due to gravity and \mathbf{j} is a vertical unit vector co-directional with the positive z -axis. The isotropic permeability of the porous medium k_p and the viscosity of the fluid μ are assumed to be

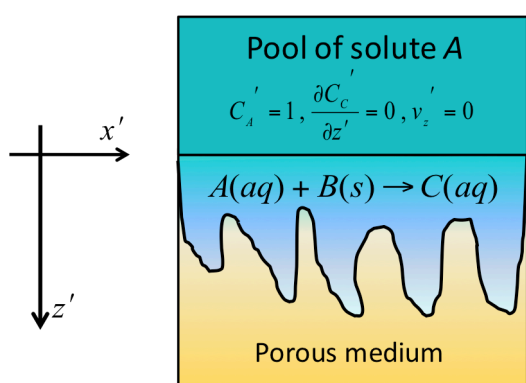


Figure 1. Solute A dissolves in underlying fluid forming a diffusive boundary layer. Dissolution enhances the local density difference between the solute-saturated fluid at the interface and the underlying pure fluid, driving finger formation and convection. Dissolved solute A reacts with reactant species B in the host rock, forming product C , which remains dissolved in the fluid. Chemical reaction alters the spatial distribution of the solute and the product, and changes the density field.

constant. The density of the fluid is assumed to be linearly dependent on the local concentrations of the solute, C_A , and the product, C_C : $\rho = \rho_r(1 + \beta_A C_A + \beta_C C_C)$; the reference density ρ_r is that of the pure fluid and the coefficients of density increase with the concentration of the solute and the product are defined as $\beta_A = (1/\rho_r)\partial\rho/\partial C_A$ and $\beta_C = (1/\rho_r)\partial\rho/\partial C_C$, respectively.

The transport of the solute A and product C is described by the advection-diffusion-reaction equations

$$\varphi \frac{\partial C_A}{\partial t} + \mathbf{v} \cdot \nabla C_A = D_A \varphi \nabla^2 C_A - k_r a C_A, \quad (3)$$

$$\varphi \frac{\partial C_C}{\partial t} + \mathbf{v} \cdot \nabla C_C = D_C \varphi \nabla^2 C_C + k_r a C_A. \quad (4)$$

Here, t is time and $k_r a$ is the reaction rate per unit volume of fluid, where the solid based kinetic rate constant is k_r and the reactive surface area per mole of the solid is a . The effective diffusivity of a dissolved species in the porous medium is taken as the product of the molecular diffusion coefficient D_i and porosity φ of the aquifer. We consider $D_A = D_C$. The effect of dispersion is neglected. Depletion of the species B is neglected. This assumption is valid when the host porous rock is rich in reactive species.

2.2 Nondimensionalization

The governing equations are non-dimensionalised using the scales $L_C = \mu D_A \varphi / k_p \Delta \rho_0 g$, $t_s = L_C^2 / D_A$, $v_s = D_A \varphi / L_C$, $p_s = \mu D_A \varphi / k_p$, and the solubility of solute A in the fluid C_s , giving

$$\nabla' \cdot \mathbf{v}' = 0, \quad (5)$$

$$\mathbf{v}' = -\nabla' p' + C'_A \mathbf{j} + \frac{\beta_C}{\beta_A} C'_C \mathbf{j}, \quad (6)$$

$$\frac{\partial C'_A}{\partial t'} + \mathbf{v}' \cdot \nabla' C'_A = \nabla'^2 C'_A - \frac{Da}{Ra^2} C'_A, \quad (7)$$

$$\frac{\partial C'_C}{\partial t'} + \mathbf{v}' \cdot \nabla' C'_C = \nabla'^2 C'_C + \frac{Da}{Ra^2} C'_A. \quad (8)$$

Here, $Da = k_r a L_z^2 / D_A \varphi$ is the Damköhler number and $Ra = k_p \Delta \rho_0 g L_z / \mu D_A \varphi$ is the solutal Rayleigh number. The maximum density contrast between the pure and solute-saturated brine is $\Delta \rho_0 = \rho_r \beta_C C_s$. The dynamics of such a reactive boundary layer is therefore fully determined by two dimensionless groups: Da/Ra^2 , which measures the timescale for convection compared to those for reaction and diffusion, and β_C/β_A , which reflects the density change induced by the product relative to that of the diffusing solute. We use the above model to study the effects of reaction kinetics on the instability and nonlinear behaviour of the boundary layer, away from chemical equilibrium, as discussed in section 3. In section 4 we discuss how the chemical equilibrium can alter the behaviour of the system.

3 Results and discussion

3.1 Time for onset of convection

The time for onset of convection has been obtained from both linear stability analysis and numerical simulations, as detailed in the appendix. Four different cases are presented in Fig. 2, covering a range of product densities: (a) $\beta_C/\beta_A = 0$, for which the product does not contribute to the density of the fluid; (b) $\beta_C/\beta_A = 1$, when the product has the same density coefficient as the reactant, (c) $\beta_C/\beta_A = 1.5$, for a heavy dissolved product; and (d) $\beta_C/\beta_A = 10$, for a very heavy dissolved product.

When the product does not contribute to the density of the fluid, the time for onset of convection is seen to increase as reaction strength increases [Fig. 2]. This can be explained by noting that as the solute is consumed by chemical reaction, the density of the layer is reduced, and the onset of convection is delayed. In a system with a product and reactant of equal density coefficients, the onset of convection is accelerated as the reaction strength increases. This behaviour results from the accumulation of product in the boundary layer and a reduction of the concentration of reactant, the latter enhancing diffusive transport and hence reducing the time for onset of convection. For a large product density coefficient ($\beta_C/\beta_A = 1.5$), the convection onset is accelerated as reaction strength increases. Here, the heavy product contributes to increase the density of the fluid and destabilises the boundary layer earlier. An even larger density contribution from the product ($\beta_C/\beta_A = 10$), reduces significantly the onset time of convection.

3.2 Convective motion

Numerical simulation was used to study the effects of the formation of a soluble product on the intensity and pattern of convective mixing. The local instantaneous speed has been computed as $\bar{v}(x', z', t') = \sqrt{u^2(x', z', t') + v^2(x', z', t')}$, while the average speed over the whole computation domain at each time instant has been obtained by evaluating $\langle \bar{v}(t) \rangle = \int_0^{L_z} \int_0^{L_x} \sqrt{u^2(x, z, t) + v^2(x, z, t)} dx dz / L_x L_z$.

The evolution of the instantaneous speed field is shown in Fig. 3. Density-coefficient ratios in the range 0 to 1.5 are investigated for $Da/Ra^2 = 1 \times 10^{-3}$ [Fig. 3(a)-(c)]. It is evident that the product density has a significant effect on both the spatial extent and the intensity of convective motion. For $\beta_C/\beta_A = 1.5$, the convective fingers penetrate deep into the domain at large time, for $\beta_C/\beta_A = 1$ only half of that depth has appreciable convection, while for $\beta_C/\beta_A = 0$ the motion is confined to the close proximity of the interface. The intensity of convection is much higher for the heavy product as evident from the colour codes. For low ($Da/Ra^2 = 0.15 \times 10^{-3}$), intermediate ($Da/Ra^2 = 1 \times 10^{-3}$) and high ($Da/Ra^2 = 2.49 \times 10^{-3}$) reaction strengths, the average speed in the whole domain, respectively, doubles, increases by tenfold, and by thousand-fold, as the density ratio increases from zero to 1.5.

It is important to note that for medium ($Da/Ra^2 = 1 \times 10^{-3}$) and large ($Da/Ra^2 = 2.49 \times 10^{-3}$) reaction strength, with $\beta_C/\beta_A = 1$ and 1.5, convective motion is maintained long-term,

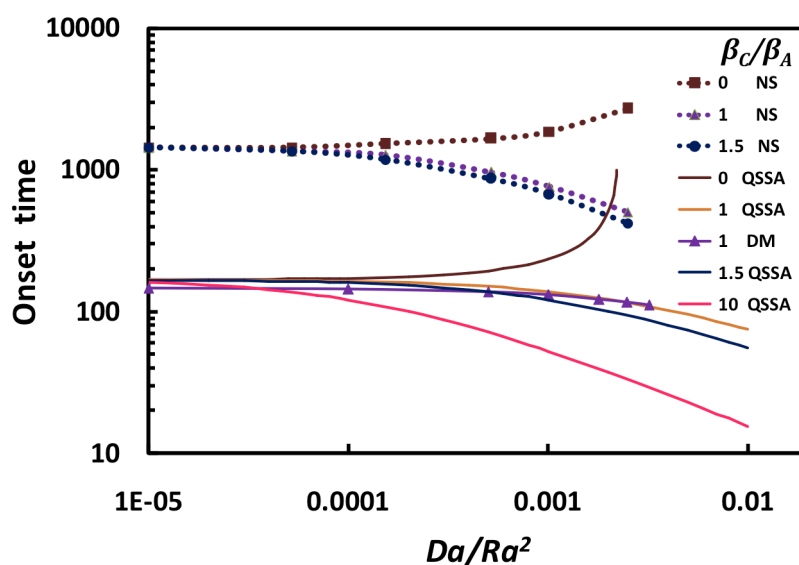


Figure 2. Time for onset of convection (dimensionless) as a function of reaction strength Da/Ra^2 , for β_C/β_A in the range 0 - 10. Results from linear stability analysis, with either quasi-steady assumptions (QSSA) or dominant-mode of the self-similar diffusion operator (DM), are presented. The dotted lines show results from nonlinear numerical simulations (NS).

even long after the fingers reach the bottom of the reservoir; this behaviour is in significant contrast to that of an inert system^{7,13}, where a substantial drop in convection intensity is observed. This behaviour is illustrated in Fig. 3(d)-(f) for intermediate reaction strength, $Da/Ra^2 = 1 \times 10^{-3}$, at a dimensionless time of $t' = 33914$. The inert system in Fig. 3(d) exhibits very weak motion, with severely curtailed finger formation and a sparse finger presence. However, for $\beta_C/\beta_A = 1$ and 1.5 [Fig. 3(e) and (f)], a large number of prominent sinking fingers are distributed throughout the domain, with new fingers forming at the interface. In these cases, the numbers of fingers are almost double of that in the inert case. For intermediate reaction strength, $Da/Ra^2 = 1 \times 10^{-3}$, with beta ratio 1 and 1.5 at a dimensionless time of $t' = 34252$, the average speed of the whole domain is maintained at $\sim 70\%$ of the peak speed obtained before the fingers reach the bottom of the domain. For high reaction strength, $Da/Ra^2 = 2.49 \times 10^{-3}$, this ratio is maintained at $\sim 75\%$. However, for the inert system at the same dimensionless time, the average speed is reduced to 30% of the maximum speed before fingers hit the bottom boundary. Thus, a reaction accompanied by heavier or equal density product formation as the solute can significantly enhance convective mixing and maintain it long term.

3.3 Solute and product concentrations

Snapshots of solute and product concentration fields are shown in Fig. 4. We consider two heavy-product scenarios

($\beta_C/\beta_A = 1.5, 10$) and compare those with the situation of a product with negligible density contribution ($\beta_C/\beta_A = 0$). At small reaction strength for $\beta_C/\beta_A = 0$ [Fig. 4(Ai)], at $t' = 2427$, tiny solute fingers are observed, which grow downwards individually. As the beta ratio increases, the fingers propagate further down within the same time frame. For $\beta_C/\beta_A = 1.5$ [Fig. 4(Bi)], fingers have a small tilt from the vertical direction indicating noticeable but minor finger interactions. Within the same time frame, for $\beta_C/\beta_A = 10$ [Fig. 4(Ci)], the solute fingers penetrate deeply into the domain and exhibit splitting at the roots. The product field exhibits a similar behaviour, albeit with the product concentration being less than that of the reactant.

For $\beta_C/\beta_A = 0$, at intermediate reaction strength, finger formation is inhibited and the fingers are confined close to the interface [Fig. 4(D)]. At large reaction strength, convection is completely halted and a diffusive-reactive boundary layer is observed with high product concentration close to the interface [Fig. 4(G)]. In contrast, for $\beta_C/\beta_A = 1.5$ and intermediate reaction strength [Fig. 4(Ei) and (Eii)], both solute and product fingers migrate further compared to case B, with solute fingers being slender and product fingers looking bulky. As reaction strength increases further [Fig. 4(H)], a drastic difference between the finger patterns for the solute and product is observed. Bulky product fingers are conveyed deep into the domain while solute fingers are very thin and remain confined to the interface. For $\beta_C/\beta_A = 10$, the reactant fingers penetrate deeper into the domain even under strong reaction.

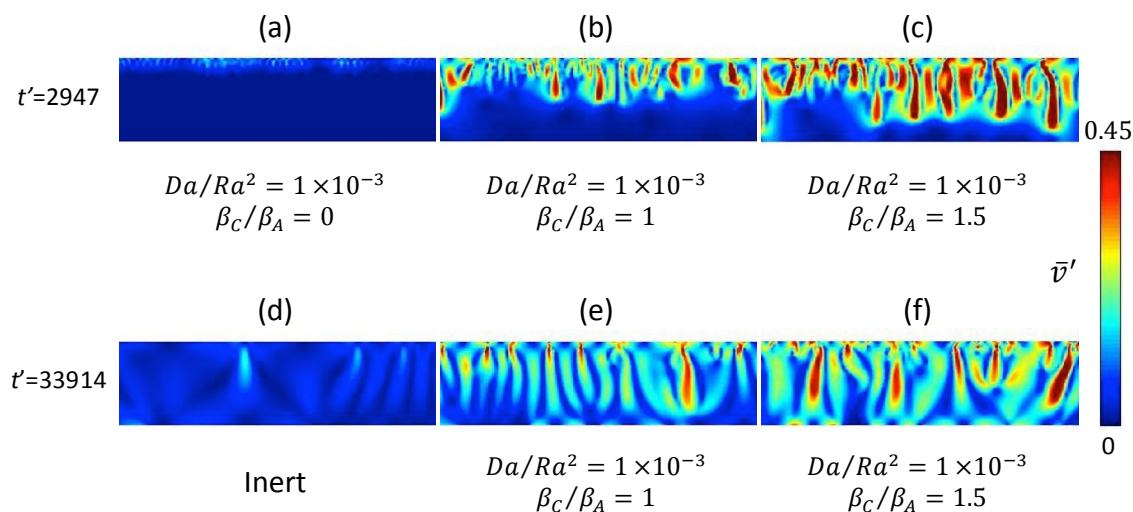


Figure 3. Snapshots of the speed field showing the effects of chemical reaction on the convective motion. (a) to (c) show enhancement of convection with an increase in density ratio. (d) shows feeble inert convection after fingers reach the bottom of the domain. (e)-(f) show that, in contrast to inert convection, chemical reaction accompanied by soluble products can maintain long-term convection, even after the fingers reach the bottom boundary.

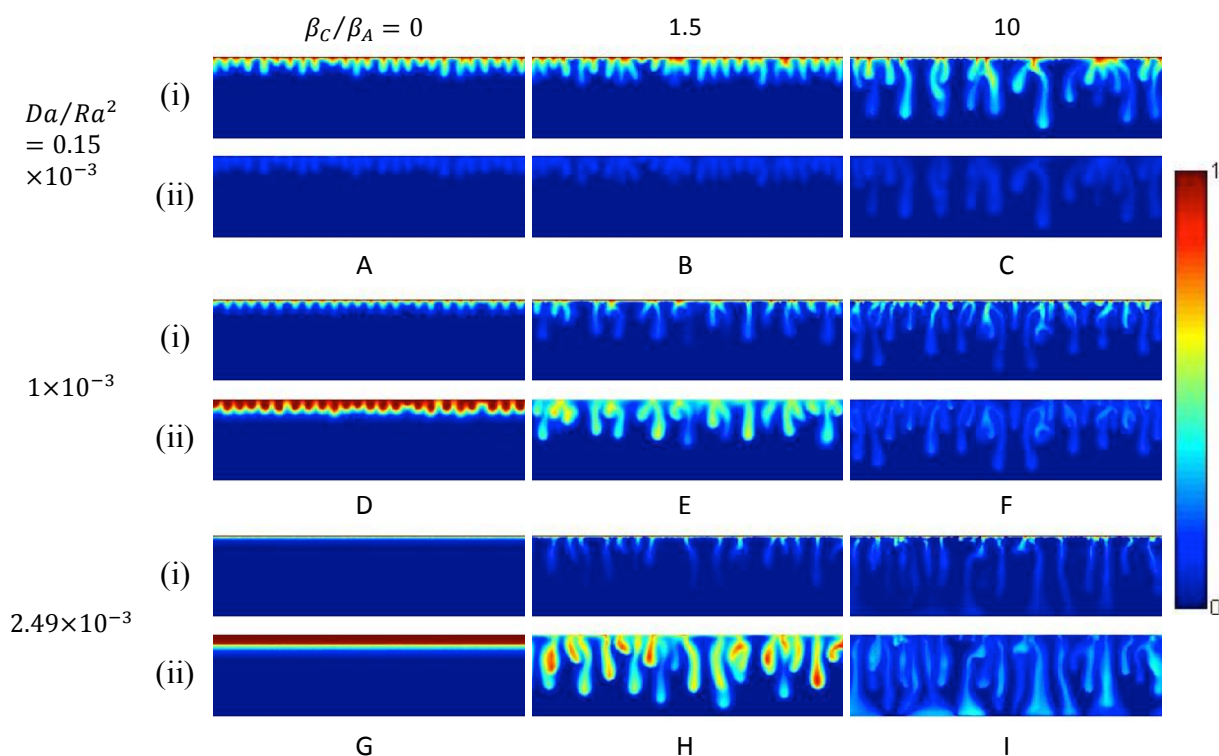


Figure 4 Snapshots showing the effect of Da/Ra^2 and β_C/β_A on (i) solute concentration and (ii) product concentration. Da/Ra^2 increases from top to bottom and β_C/β_A increases from left to right. Snapshots are shown at dimensionless times $t'=2427$ for A, B, C, E and H; $t'=3467$ for D and G; $t'=1126$ for F and I.

In contrast to the case with density ratio 1.5, product fingers are slender and have lower concentration. This is a consequence of the presence of heavy product, which elongates the fingers and enhances lateral diffusion.

There are striking similarities and differences in the finger patterns between situations with (a) low reaction strength and large beta ratio [Fig. 4(C)] and (b) large reaction strength with small beta ratio [Fig 4(H)]. It is noteworthy that in both the cases plumes penetrate deep in the reservoir with comparable speed. However, for case C the reactant concentration is more prominent than product concentration, while for case H, reactant fingers are small and slim, and product-rich fingers are conveyed down, suggesting the flow is primarily driven by the product.

It is important to consider the depth of the chemically active zone in the reservoir. Chemical reaction introduces a complex, nonlinear competition between reactant depletion and its transport by convection, promoted by the density of a fluid with spatially varying proportions of reactant and products. Our reactive transport simulation suggests that rapid chemical reactions are confined to a shallow region close to the top of the reservoir where the reactant remains localised

[Fig. 4(H)]. The deeper part of the reservoir remains chemically inactive; here inert, product-rich fingers prevail and mass transfer occurs through convection and diffusion. For slow chemical reactions and large density ratio, long-lived reactant fingers descend deeper into the domain and a greater part of the reservoir is chemically active. For $Da/Ra^2 = 2.49 \times 10^{-3}$ with $\beta_C/\beta_A = 1.5$, the solute is restricted within half of the total depth of the simulation domain, while for $Da/Ra^2 = 1 \times 10^{-3}$ with the same density ratio and for $Da/Ra^2 = 2.49 \times 10^{-3}$ with $\beta_C/\beta_A = 10$, the solute is distributed throughout the whole domain.

The above results suggest that it is worth resolving the finger patterns into solute and product concentration components for a comprehensive understanding of the reactive-convective mixing patterns. The vertical spreading of the solute and the product is further quantified in the horizontally averaged concentration profiles, presented in Fig. 5 and Fig. 6, respectively. Horizontally averaged concentration profiles for the solute and the product are defined as $\langle C_A'(z', t') \rangle = \int_0^{L_x'} C_A'(x', z', t') dx' / L_x'$, and $\langle C_C'(z', t') \rangle = \int_0^{L_x'} C_C'(x', z', t') dx' / L_x'$. These plots reveal valuable

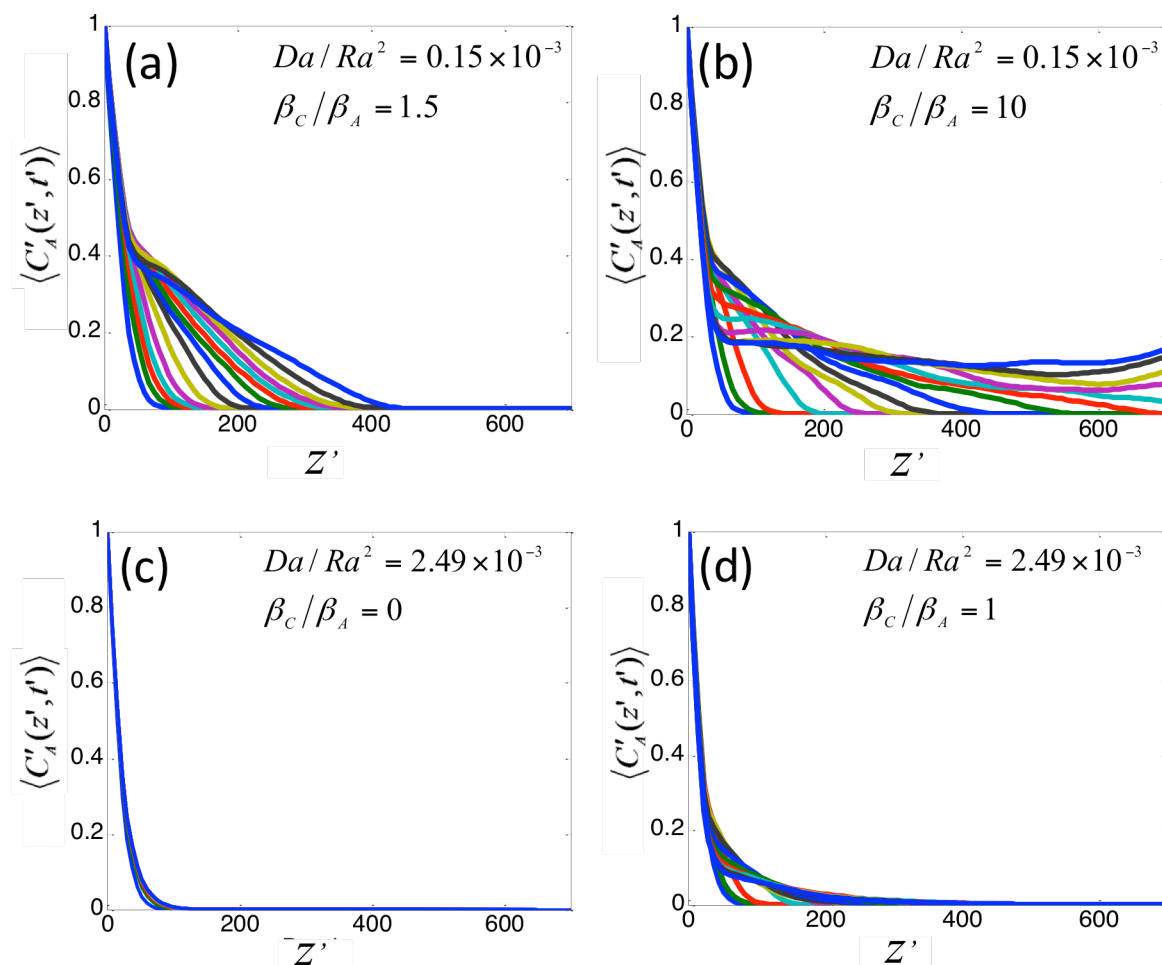


Figure 5. Horizontally-averaged solute concentration versus depth for times between $t' = 87$ and $t' = 3727$ with time interval $\Delta t' = 260$ (dimensionless). The boundary layer grows from left (top of the domain) to right (bottom of the domain).

information about the early-time growth of the boundary layer and long-term dynamic behaviour of the fingering region. Situations with four different combinations of Da/Ra^2 and β_C/β_A are discussed. Each curve represents one time instant, and the same time range is covered in all the plots. The boundary layer grows from the top interface (left) to the bottom of the domain (right) in the figures. At small reaction strength, $Da/Ra^2 = 0.15 \times 10^{-3}$ and $\beta_C/\beta_A = 1.5$ [Fig. 5(a)], upon onset of convection, swelled regions start appearing in concentration profiles. This structure is maintained for some time, after which the concentration gradient is sharpened close to the interface as more solute is conveyed down from the interface. This behaviour is similar to that for inert situations reported by Andres and Cardoso.²⁷ As the product density increases ($\beta_C/\beta_A = 10$, [Fig. 5(b)]), convection is established more rapidly. More prominent sharpening of the concentration gradient is observed demonstrating pronounced

convective removal of solute from the interface and its effective transport towards the bottom of the domain.

As reaction strength increases, for density ratio zero, the swelling and sharpening dynamics is halted, and a diffusive-reactive solute profile prevails close to the interface [Fig. 5(c)]. Contrariwise, for beta ratio 1, swelling starts earlier owing to an earlier onset of convection and the concentration plots fold to substantial extents due to intense motion [Fig. 5(d)]. Despite the pronounced convection, solute does not seem to accumulate near the bottom boundary owing to its rapid consumption by chemical reaction. Solute concentration is restricted to a region up to dimensionless length 300.

At small time, the product concentration remains restricted to a small region close to the upper boundary. The diffusive-reactive boundary layer evolves, with a maximum product concentration at the interface and a monotonic decrease with distance from it. As time progresses, both the thickness of the product region and the product concentration at the interface

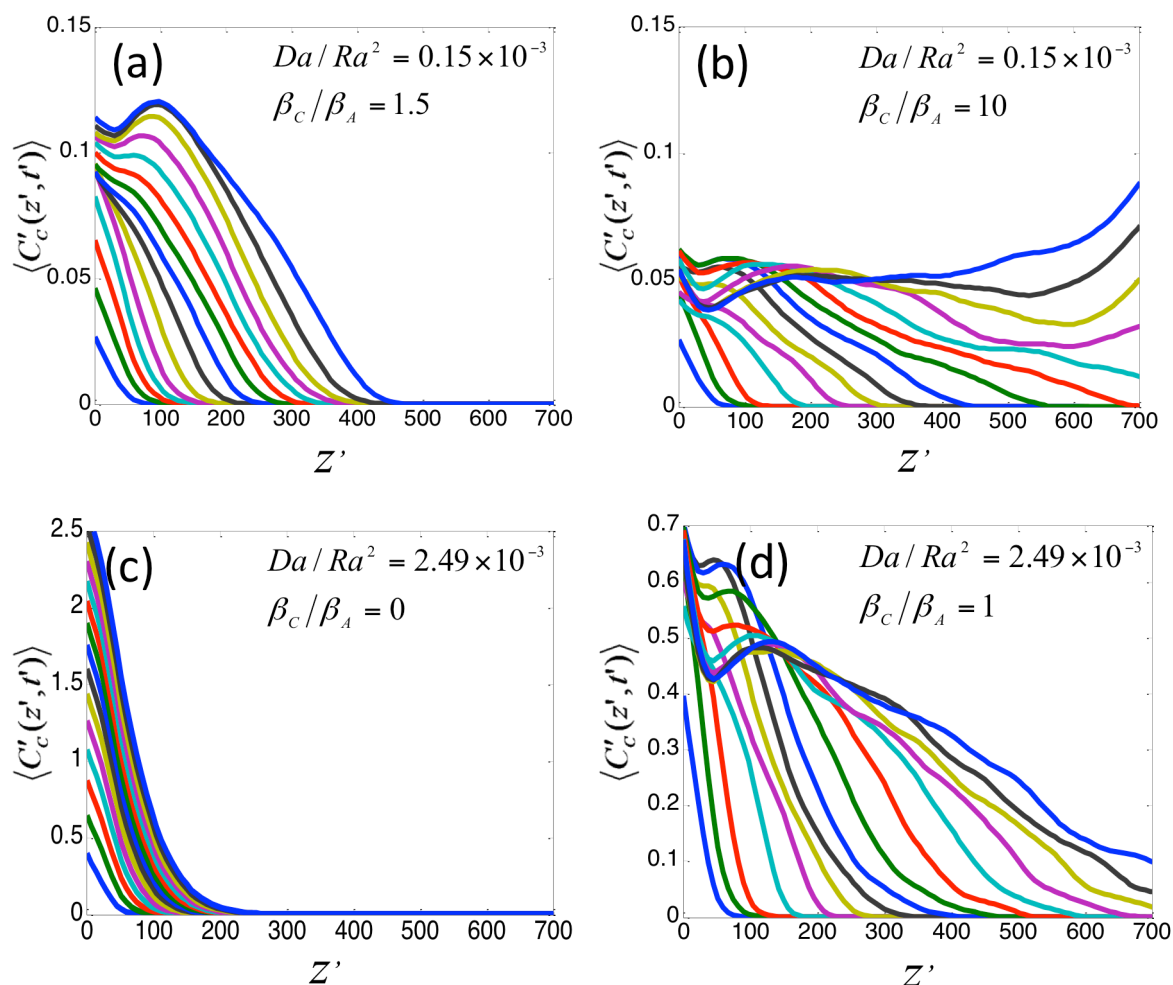


Figure 6. Horizontally -averaged product concentration versus depth for times between $t' = 87$ and $t' = 3727$ with time interval $\Delta t' = 260$ (dimensionless). The boundary layer grows from left (top of the domain) to right (bottom of the domain).

increase. At small reaction strength, $Da/Ra^2 = 0.15 \times 10^{-3}$ and $\beta_C/\beta_A = 1.5$ [Fig. 6(a)], upon onset of convection, the product concentration at the interface increases more slowly, while products accumulate slightly away from the interface. A bulge in the product concentration profile develops which grows and moves downward with time. For large density ratio [Fig. 6(b)], upon onset of convection, the interface concentration first decreases and then remains virtually constant as the product is quickly transported down. The interface concentration is limited to a smaller value and the profile is relatively uniform. At large time, the product accumulates at the impermeable base.

Fig 6(c) shows the diffusive-reactive product concentration profile for large reaction strength ($Da/Ra^2 = 2.49 \times 10^{-3}$) with density ratio zero. A monotonic product concentration profile continues increasing with time. The interface concentration increases much faster than for the low reaction strength under

diffusive transport ([Fig. 6(a)] at small time). At the same large reaction strength, even with the equal density contribution from the product as the solute [Fig 6(d)], a remarkably different concentration profile is observed, owing to the development of convection. In contrast to the solute concentration profile [Fig 5(d)], the product is transported deep into the domain.

3.4 Rate of solute dissolution at the top interface

The presence of a heavy reaction product can have considerable impact on the rate of dissolution of solute at the top interface, as demonstrated in Fig. 7. The solute mass flux dissolving at the top boundary is obtained from $J = (D_A \varphi / L_x) \int_0^{L_x} \partial C_A / \partial z|_{z=0} dx$, or in dimensionless form, $J' = J L_c / D_A \varphi C_s$. Reaction strengths ranging from $Da/Ra^2 = 0 - 2.49 \times 10^{-3}$ are investigated for $\beta_C/\beta_A = 0, 1$ and 1.5.

At early time, in the diffusion-reaction regime, all flux curves decay towards a minimum value, as the solute concentration gradient decreases owing to vertical diffusion, [Fig. 7(a)]. The flux is mainly determined by the reaction strength and is independent of the density ratio. As reaction strength increases, the flux curves shift up and decay at much slower rate as the concentration gradient is sharpened owing to more pronounced consumption of solute.

Following onset of convection, the dissolution flux recovers. This is illustrated for each Da/Ra^2 by the separation of the curves, first for the highest beta ratio, followed by the other lower ratios [Fig 7(a)]. The flux steadily increases owing to convective transport and reaches a local maximum. For the

inert system, this is termed the ‘flux growth’ regime.¹³

For the reactive system with beta ratio zero, the flux increases with reaction strength, but the curves become flatter owing to suppression of finger formation. In contrast, for $\beta_C/\beta_A = 1, 1.5$, the flux subsequently drops as fingers interact to a statistically constant value with some fluctuations. The flux is larger for $\beta_C/\beta_A = 1.5$, than that for $\beta_C/\beta_A = 1$ owing to the presence of more fingers (see section 3.5) that quickly propagate downward. The constant flux is reached at an earlier time as the density ratio increases. For higher reaction strength, the flux is maintained at a higher level owing to a more pronounced removal of the solute from the interface by chemical reaction and by advection of a larger number of reactive fingers. At this statistically constant flux regime, fingers reach the bottom of the domain. It has been verified by doubling the depth of the simulation domain that the dissolution flux remains unaffected by the presence of the bottom boundary for intermediate ($Da/Ra^2 = 1 \times 10^{-3}$) and large ($Da/Ra^2 = 2.49 \times 10^{-3}$) reaction strengths. For low reaction strength ($Da/Ra^2 = 0.15 \times 10^{-3}$), following this regime, at large time, the flux gradually decreases (not shown).

The total amount of trapped solute is obtained by integrating the flux J over time curve. For intermediate ($Da/Ra^2 = 1 \times 10^{-3}$) and high ($Da/Ra^2 = 2.49 \times 10^{-3}$) reaction strengths, with $\beta_C/\beta_A = 1.5$, the total amount of solute uptake increases by 100% and 169%, respectively, compared to the inert case.

3.5 Formation and dynamic evolution of finger structures

The formation and dynamic evolution of finger patterns are quantified by the power-averaged, instantaneous finger number (see appendix D), $n(t)$, in the whole simulation domain [Fig 8(a)]. The effects of chemical reaction on the linear and non-linear finger behaviour are further characterized by measuring the deviation between the average finger number in the reactive and inert simulations at a given time, $n(t) - n_{inert}(t)$, [Fig 8(b)].

At early times, the finger number increases and reaches a peak value. This maximum number corresponds to the local minimum in the flux curve. This is the finger formation period. As reaction strength increases, the finger number increases and convection develops earlier. The finger number at the time of onset of convection has been found to increase to a small extent as the density ratio increases from 1 to 1.5 [Fig. 8(b)]. Our simulations with larger density contribution from product, $\beta_C/\beta_A = 5, 10$ (not shown), indicate more substantial increase in finger number. From the above diagram, it is also seen that the reaction strength (Da/Ra^2) has a more prominent effect on finger number at the onset than the density ratio.

Beyond the formation period, the fingers grow individually for some time, after which merger occurs, promoted by the interaction of the velocity fields of adjacent fingers¹⁹. As reaction strength increases, the finger number is seen to reduce sharply owing to effective finger coalescence, as clearly visible in Fig 8(b). In this merging regime, the finger interaction

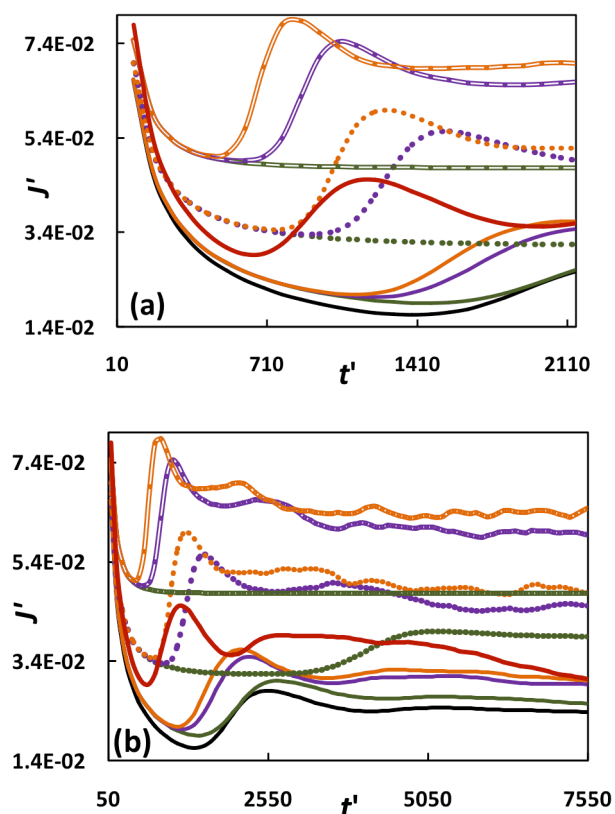


Figure 7. Mass flux of solute dissolving at the top boundary for different combinations of Da/Ra^2 and β_C/β_A : (a) small-time behaviour; (b) small- and large-time behaviours. The inert flux is shown as the black solid line. Reactive cases for $Da/Ra^2 = 0.15 \times 10^{-3}$, 1×10^{-3} and 2.49×10^{-3} are represented by solid, dotted and compound lines, respectively; $\beta_C/\beta_A = 0, 1$ and 1.5 are represented by green, purple and orange lines, respectively. The application to the geo-storage of carbon dioxide in carbonate rich aquifers is shown as the red solid line.

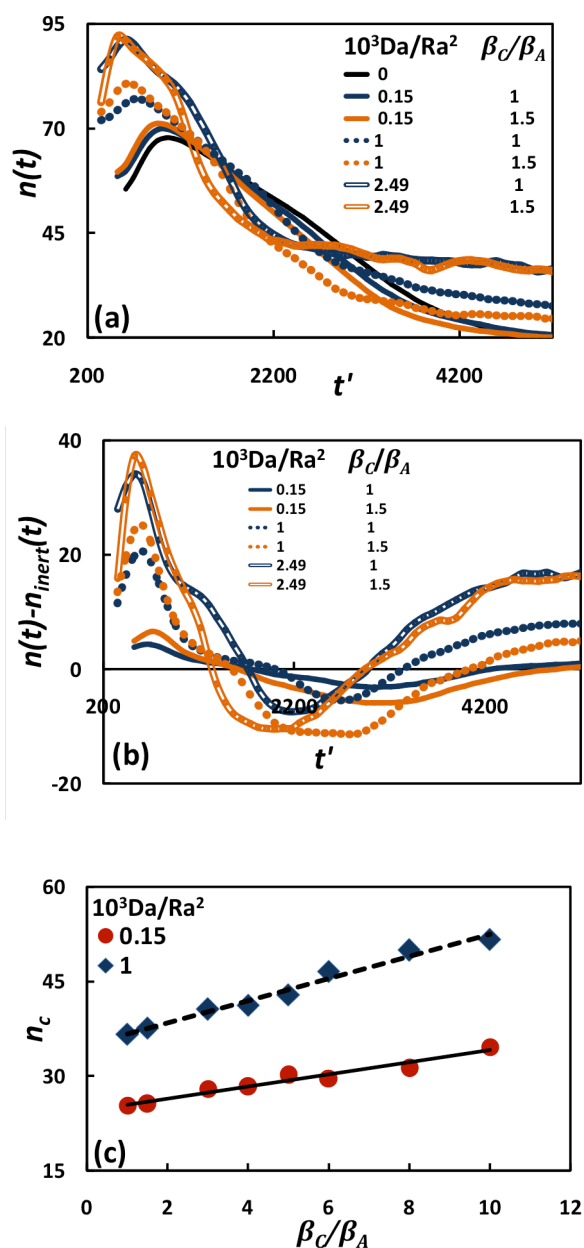


Figure 8. Effect of Da/Ra^2 and β_c/β_A on formation and evolution of finger patterns: (a) Instantaneous finger number $n(t)$, (b) deviation between finger number in reactive and inert systems, and (c) effect of beta ratio on characteristic finger number, for two different Da/Ra^2 . Linear trend lines are drawn through the data points.

becomes stronger as the beta ratio rises, leading to a larger solute dissolution flux at the interface. At larger time, the finger number decreases further, subsequently remaining constant and maintaining the flux at a steady level. In this regime, a stronger reaction favours a higher finger number and

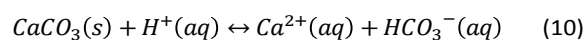
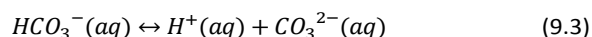
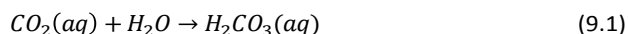
a larger reactive-advective solute dissolution flux at the interface.

The effect of the density ratio on the fingering pattern is further quantified by measuring the finger number corresponding to the time at which fingers reach 50% of the depth of the reservoir. The characteristic finger number, n_c , is plotted against β_c/β_A , for two different Da/Ra^2 in Fig 8(c). The characteristic finger number increases linearly as the density ratio increases, in accord with the large number of slender fingers visible in the concentration contours [Fig 4(F)].

The formation of more fingers when the density ratio is increased may be explained as follows. In the nonlinear regime, fingers merge with their adjacent neighbours reducing the wave number. In the troughs of the wave solute diffuses from the top into the lower layers and undergoes reaction. When this local boundary layer becomes sufficiently heavy, instability develops, new fingers form transporting dense material to larger depth. As the density coefficient ratio increases, conversion of the solute to large density product enhances the development of the instability. For inert convection, the most unstable wave number at the onset of instability has been reported to vary linearly with Rayleigh number, and therefore linearly with the density contrast.^{5,8} At the onset of convection, our simulations for the reactive system also suggest a linear increase in finger number with increase in ratio of the density-coefficient of the product to the solute (not shown). We conjecture then that the continuous process of development of incipient instability following finger merger, described above, is responsible for the linear increase of the wave number with the density ratio observed in the nonlinear regime.

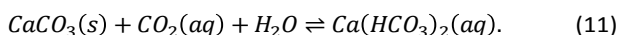
4. Application

Finally, we discuss the application of our findings to the storage of carbon dioxide in a carbonate-rich saline aquifer. Marini⁴⁰ describes the dissolution reaction of limestone in the presence of aqueous carbon dioxide to produce soluble calcium bicarbonate in such a reservoir. Dissolved carbon dioxide in brine forms carbonic acid, which dissociates into hydrogen, bicarbonate and carbonate ions. In the presence of the hydrogen ion, calcite dissolves forming calcium and bicarbonate ions.⁴⁰



The ratio of the concentrations of carbonate and bicarbonate ions at pH=8 is less than 0.01 and even smaller under acidic

conditions.⁴⁰⁻⁴¹ Therefore, by neglecting equation (9.3), the above reactions can be combined as



The species $\text{CO}_2(aq)$, $\text{CaCO}_3(s)$ and $\text{Ca}(\text{HCO}_3)_2(aq)$ are represented by A , B and C , respectively, in our model. Reaction (11) can lead to an order of magnitude increase in the density of the fluid compared to that associated with the dissolution of carbon dioxide in brine ($\beta_C/\beta_A \sim 40$).^{5,42-43} Our analysis can therefore be applied to such situation.

For reaction (9.1), the reaction rate constant has been reported as $\sim 10^{-2} \text{s}^{-1}$ and for (9.2), even faster.⁴⁴ Following kinetic data of Marini,⁴⁰ we estimate the reaction rate constant for reaction (10) as $\sim 10^{-4} \text{s}^{-1}$. Therefore, the dissolution reaction (10) has the slowest rate among the reactions (9)-(10) and is therefore the rate-determining step. Using kinetic data of Marini,⁴⁰ the overall reaction kinetics can be approximated as first-order with respect to aqueous carbon dioxide. With reservoir permeability $k_p = 5 \times 10^{-12} \text{m}^2$ and porosity $\varphi = 0.3$, we estimate $\text{Da}/\text{Ra}^2 = 0.1$. Numerical simulations for $\text{Da}/\text{Ra}^2 = 0.1$ and $\beta_C/\beta_A = 10$, suggest almost instantaneous onset of convection, within less than one hour after injection of carbon dioxide into the aquifer. The convective fingers are expected to advance downwards in the reservoir at a rate of $\sim 2 \text{cm/hr}$.

The above model is suitable for the situations where the chemical reaction does not reach equilibrium since only the forward reaction is considered. This is a valid assumption for slow geochemical reactions. In general, geochemical reactions between aqueous carbon dioxide and porous rocks have slow reaction rates.⁴² However, for situations where the rate of the chemical reaction is moderately high, as in the example above, the geochemical reaction may reach chemical equilibrium, which will restrict further dissolution of the rock matrix. Our numerical results do indeed show that the local concentrations of calcium bicarbonate and dissolved carbon dioxide can reach equilibrium. Therefore, a modification of the above model is required to incorporate the backward reaction.

A backward reaction has been added to the governing balances as follows:

$$\nabla \cdot \mathbf{v} = 0, \quad (12)$$

$$\mathbf{v} = -\frac{k_p}{\mu} (\nabla p - \rho_r \beta_A C_A \mathbf{g}) - \rho_r \beta_C C_C \mathbf{g}), \quad (13)$$

$$\varphi \frac{\partial C_A}{\partial t} + \mathbf{v} \cdot \nabla C_A = D_A \varphi \nabla^2 C_A - k_{rA} a C_A + k_{rC} C_C, \quad (14)$$

$$\varphi \frac{\partial C_C}{\partial t} + \mathbf{v} \cdot \nabla C_C = D_C \varphi \nabla^2 C_C + k_{rA} a C_A - k_{rC} C_C. \quad (15)$$

Here, $k_{rA} a$ and k_{rC} are the rate constants for the forward and backward reactions, respectively. The magnitude of the backward reaction rate constant k_{rC} is calculated from the equilibrium between the local concentrations of calcium bicarbonate and carbon-dioxide(aq):

$$[\text{Ca}(\text{HCO}_3)_2] = [\text{CO}_2(aq)]^{\frac{1}{3}} \frac{(K_1 K_2 K_4)^{\frac{1}{3}}}{4^{\frac{1}{3}}}. \quad (16)$$

Here, K_1, K_2, K_4 are equilibrium constants for reactions (9.1), (9.2) and (10), respectively.⁴⁵

Numerical simulations with the modified model for $\beta_C/\beta_A = 40$, predicts the time for onset of convection to be 3.3 days. The convective fingers are expected to advance downwards in the reservoir at a rate of $\sim 5 \text{cm/day}$. Before the fingers reach the bottom of the domain, the solute dissolution flux (dimensionless) at the interface [Fig.7(b)] is ~ 1.5 times that for the inert system. Under reservoir conditions, the carbon-dioxide dissolution flux at the CO_2 -brine interface is predicted to be $100 \text{ ton km}^{-2} \text{ day}^{-1}$ before the fingers reach the bottom of the reservoir; this is almost 1.2 times the flux predicted by Szulczewski *et al.*⁴⁶ for similar reservoir properties without geochemical reactions. At large time, the flux gradually decreases, suggesting a shutdown of convection in the long term.

5. Conclusions

A theoretical and numerical study of the development of convection in a diffusive boundary layer, undergoing a first-order chemical reaction, was performed. Scaling of the governing volume, momentum and chemical balances showed that the boundary-layer behaviour is fully determined by two dimensionless groups: the ratio of the Damköhler number and the square of the solutal Rayleigh number, Da/Ra^2 , and the coefficient of density change of the reaction product species compared to that of the diffusing solute, β_C/β_A . It was shown that the state of mixing in the convective layer depends strongly on the magnitudes of Da/Ra^2 , and β_C/β_A . While β_C/β_A controls more strongly the time for onset of convection, Da/Ra^2 has more effect on the dissolution flux.

Our results show that the presence of the soluble product, even of equal density to the solute, can substantially destabilize and alter the nonlinear, dynamic behaviour of the boundary layer, compared to that for inert convection. Importantly, the situations with larger β_C/β_A , are characterized by faster moving fingers, accompanied by larger wave numbers. Additionally, higher Da/Ra^2 increases the number of fingers at instability and enhances dynamic finger interactions as well. Under slow reaction conditions, solute rich fingers develop slowly and remain almost homogeneous in composition. For a rapid chemical reaction, with moderate β_C/β_A , heavy product-rich fingers travel deep into the domain, but remain rich in solute close to the interface. As β_C/β_A increases, the large density contribution from the product elongates both the solute and product fingers, resulting in deeper, chemically active domain. These complex hydrodynamic and chemical interactions lead to accelerated mass transport in the reactive system compared to that in the inert. An increase in Da/Ra^2 from zero to 2.49×10^{-3} doubles the dissolution flux.

Our findings were applied to the geo-storage of carbon dioxide in a carbonate saline aquifer. It was shown that the solubility restrictions of calcium carbonate curtail the increase of CO_2 flux to 50% of that in the inert system.

Acknowledgements

P.G. gratefully acknowledges the Dr. Manmohan Singh Scholarship from St. John's College, Cambridge and the grant of study Leave from Jadavpur University, Kolkata, India. We thank Csaba Katai and Phanos Anastasiou, undergraduate Research Project students, for carrying out some of the numerical simulations.

Appendix

A. Linear stability analysis

The porous medium is considered to be infinite in the horizontal direction (x') and semi-infinite in vertical direction (z' , taken as positive downward). This assumption is valid while the finger penetration depth is smaller than the domain depth, i.e., for small time. At time $t' = 0$, the entire domain is quiescent, and solute and product free, i.e. $\mathbf{v}'(x', z', 0) = 0$, $C'_A(x', z', 0) = 0$, and $C'_C(x', z', 0) = 0$.

The linear stability analysis has been carried out using two methods: (a) the quasi-steady state approximation and (b) considering the dominant mode of the self-similar diffusion operator. Both these methods have previously been applied for inert systems.^{8,11} The dominant mode solution does not require the quasi-steady state approximation and has been shown to predict accurately the critical time for the onset of convection for inert systems.⁸ However, for an inert system the dominant-mode solution has been found to be less accurate at large time and solutions based on the quasi-steady state approximation have been suggested.⁸ These two methods are therefore mutually complementary since the quasi-steady condition is applicable when time is large. We apply both methods to obtain solutions for the reactive system where the product of the chemical reaction alters the density field. We obtain the time for onset of convection from each solution.

Linear stability equations: Concentration, velocity components and pressure in the governing equations (5) to (8) are decomposed into non-convective base-state and perturbation components such that

$$C'_A = C_{Ab} + \hat{C}_A, \quad (17a)$$

$$C'_C = C_{Cb} + \hat{C}_C, \quad (17b)$$

$$u' = u_b + \hat{u}, \quad (17c)$$

$$v' = v_b + \hat{v}, \quad (17d)$$

$$p' = p_b + \hat{p}. \quad (17e)$$

Here, subscript b denotes base state and caret denotes perturbation components. The perturbation equations are linearized and rearranged to eliminate pressure and horizontal-velocity component such that (all variables are in dimensionless form, superscript $'$ is dropped for simplicity)

$$\frac{\partial^2 \hat{v}}{\partial x^2} + \frac{\partial^2 \hat{v}}{\partial z^2} = \frac{\partial^2 \hat{C}_A}{\partial x^2} + \frac{\beta_C}{\beta_A} \frac{\partial^2 \hat{C}_C}{\partial x^2}, \quad (18)$$

$$\frac{\partial \hat{C}_A}{\partial t} + \hat{v} \frac{\partial C_{Ab}}{\partial z} = \frac{\partial^2 \hat{C}_A}{\partial x^2} + \frac{\partial^2 \hat{C}_A}{\partial z^2} - \frac{Da}{Ra^2} \hat{C}_A, \quad (19)$$

$$\frac{\partial \hat{C}_C}{\partial t} + \hat{v} \frac{\partial C_{Cb}}{\partial z} = \frac{\partial^2 \hat{C}_C}{\partial x^2} + \frac{\partial^2 \hat{C}_C}{\partial z^2} + \frac{Da}{Ra^2} \hat{C}_A. \quad (20)$$

The solutions are decomposed into normal modes in the horizontal direction with wave number k as

$$\hat{v} = v_0(z, t)e^{ikx}, \quad (21a)$$

$$\hat{C}_A = C_{A0}(z, t)e^{ikx}, \quad (21b)$$

$$\hat{C}_C = C_{C0}(z, t)e^{ikx}. \quad (21c)$$

Using (21) in (18-20), the following equations are obtained:

$$\frac{\partial^2 v_0}{\partial z^2} - k^2 v_0 = -k^2 C_{A0} - \frac{\beta_C}{\beta_A} k^2 C_{C0}, \quad (22)$$

$$\frac{\partial C_{A0}}{\partial t} + v_0 \frac{\partial C_{Ab}}{\partial z} = -k^2 C_{A0} + \frac{\partial^2 C_{A0}}{\partial z^2} - \frac{Da}{Ra^2} C_{A0}, \quad (23)$$

$$\frac{\partial C_{C0}}{\partial t} + v_0 \frac{\partial C_{Cb}}{\partial z} = -k^2 C_{C0} + \frac{\partial^2 C_{C0}}{\partial z^2} + \frac{Da}{Ra^2} C_{C0}. \quad (24)$$

After coordinate transformation with $\eta = z/2\sqrt{t}$, equations (22)-(24) become

$$\frac{1}{4t} \frac{\partial^2 v_0}{\partial \eta^2} - k^2 v_0 = -k^2 C_{A0} - \frac{\beta_C}{\beta_A} k^2 C_{C0}, \quad (25)$$

$$t \frac{\partial C_{A0}}{\partial t} = \left(\frac{1}{4} \frac{\partial^2}{\partial \eta^2} + \frac{\eta}{2} \frac{\partial}{\partial \eta} \right) C_{A0} - \left(k^2 + \frac{Da}{Ra^2} \right) C_{A0} t - \frac{v_0}{2} \sqrt{t} \frac{\partial C_{Ab}}{\partial \eta}, \quad (26)$$

$$t \frac{\partial C_{C0}}{\partial t} = \left(\frac{1}{4} \frac{\partial^2}{\partial \eta^2} + \frac{\eta}{2} \frac{\partial}{\partial \eta} \right) C_{C0} - k^2 C_{C0} t + \frac{Da}{Ra^2} C_{A0} t - \frac{v_0}{2} \sqrt{t} \frac{\partial C_{Cb}}{\partial \eta}. \quad (27)$$

Quasi-steady state approximation (QSSA): Under the quasi-steady state approximation (QSSA), for a given t , we express the concentration perturbations as

$$[C_{A0}(\eta, t), C_{C0}(\eta, t)] = [C_{A0}^*(\eta), C_{C0}^*(\eta)] \exp(\sigma t). \quad (28)$$

Then, the linear stability equations (25)-(27) are degenerated as

$$\left(\frac{1}{4} \frac{d^2}{d\eta^2} - k^2 t \right) v_0 = -k^2 t \left(C_{A0}^* + \frac{\beta_C}{\beta_A} C_{C0}^* \right), \quad (29)$$

$$\sigma t C_{A0}^* = \left(\frac{1}{4} \frac{d^2}{d\eta^2} + \frac{\eta}{2} \frac{d}{d\eta} \right) C_{A0}^* - \left(k^2 t + \frac{Da}{Ra^2} t \right) C_{A0}^* - \frac{v_0}{2} \sqrt{t} \frac{\partial C_{Ab}}{\partial \eta} \Big|_t, \quad (30)$$

$$\sigma t C_{C0}^* = \left(\frac{1}{4} \frac{d^2}{d\eta^2} + \frac{\eta}{2} \frac{d}{d\eta} \right) C_{C0}^* - \left(k^2 t C_{C0}^* - \frac{Da}{Ra^2} t C_{A0}^* \right) - \frac{v_0}{2} \sqrt{t} \frac{\partial C_{Cb}}{\partial \eta} \Big|_t, \quad (31)$$

with the boundary conditions, $v_0 = C_{A0}^* = C_{C0}^* = 0$ at $\eta = 0$ and $v_0 \rightarrow 0$, $dC_{A0}^*/d\eta \rightarrow 0$ and $dC_{C0}^*/d\eta \rightarrow 0$ as $\eta \rightarrow \infty$. Here, $\partial C_{Ab}/\partial \eta|_t$ and $\partial C_{Cb}/\partial \eta|_t$ represent the base concentration gradients at a given time t . This eigenvalue problem was solved numerically by employing the outward shooting method explained in Kim and Choi's work.^{11, 28}

Dominant mode analysis: Summation of equations (26) and (27) yields

$$t \frac{\partial C_{AC0}}{\partial t} = \left(\frac{1}{4} \frac{\partial^2}{\partial \eta^2} + \frac{\eta}{2} \frac{\partial}{\partial \eta} \right) C_{AC0} - k^2 C_{AC0} t - \frac{v_0}{2} \sqrt{t} \frac{\partial C_{ACb}}{\partial \eta}. \quad (32)$$

Here, $C_{AC0} = C_{A0} + C_{C0}$ and $C_{ACb} = C_{Ab} + C_{Cb}$. The non-convective base state profiles C_{Ab} and C_{Cb} satisfy the boundary conditions $C_{Ab} = 1$, $\partial C_{Cb}/\partial \eta = 0$ at $\eta = 0$ and $C_{Ab} \rightarrow 0$, $C_{Cb} \rightarrow 0$

as $\eta \rightarrow \infty$. We consider the perturbation boundary conditions $C_{A0} = 0, C_{C0} = 0$, i. e., $C_{AC0} = 0$ at $\eta = 0$ and $C_{A0} \rightarrow 0, C_{C0} \rightarrow 0$, i. e., $C_{AC0} \rightarrow 0$ as $\eta \rightarrow \infty$.

The streamwise operator of C_{AC0} is

$$\mathcal{L} = \left(\frac{1}{4} \frac{\partial^2}{\partial \eta^2} + \frac{\eta}{2} \frac{\partial}{\partial \eta} \right), \quad (\eta \in (0, \infty)). \quad (33)$$

Therefore, C_{AC0} can be expanded as

$$C_{AC0} = \sum_{n=1}^{\infty} A_{ACn}(t) \psi_{ACn}(\eta), \quad (34)$$

with $\mathcal{L} \psi_{ACn} = \lambda_n \psi_{ACn}(\eta)$. The eigen functions ψ_{ACn} are Hermite polynomials in a semi-infinite domain with weight functions $\exp(-\eta^2)$ with the associated eigenvalues $\lambda_n = -n$.⁸ Following Riaz et al.,⁸ it can be shown that in the limit of zero-wave number, the first mode decays at the slowest rate compared to the other modes and is therefore the dominant mode.

Considering the dominant mode of the perturbation concentration, $C_{AC0} = A_{AC1} \eta \exp(-\eta^2)$, we define the growth rate of perturbation as

$$\sigma_1 = \frac{1}{A_{AC1}} \frac{dA_{AC1}}{dt} = -\frac{1}{t} - k^2 - \frac{1}{2\sqrt{t}} \frac{\int_0^{\infty} \frac{v_0}{A_{AC1}} \left(\frac{\partial C_{ACb}}{\partial \eta} \right) d\eta}{\int_0^{\infty} \eta \exp(-\eta^2) d\eta}, \quad (32)$$

following Riaz et al.⁸ For $\beta_C/\beta_A = 1$, v_0 is obtained from equation (25) as

$$\frac{1}{4t} \frac{\partial^2 v_0}{\partial \eta^2} - k^2 v_0 = -k^2 C_{AC0} \quad (33)$$

with boundary conditions $v_0 = 0$ at $\eta = 0$ and $v_0 \rightarrow 0$ as $\eta \rightarrow \infty$. Therefore, for $\beta_C/\beta_A = 1$, the above growth rate can be obtained semi-analytically.

B. Nonlinear numerical simulations

Initial and boundary conditions: At time $t' = 0$, the entire domain is quiescent, and is solute and product free, i.e. $\mathbf{v}'(x', z', 0) = 0$, $C'_A(x', z', 0) = 0$, and $C'_C(x', z', 0) = 0$. The top boundary is impermeable to the product and the fluid, and has the maximum concentration of solute: $\partial C'_C/\partial z'(x', 0, t') = 0$, $v'(x', 0, t') = 0$, and $C'_A(x', 0, t') = 1$. Here, v' is the vertical component of the velocity vector in dimensionless form. Finite domain depth $L'_{z'}$ and domain width $L'_{x'}$ are considered. The bottom boundary is assumed impermeable to flow, solute and product, such that $v'(x', L'_{z'}, t') = 0$, $\partial C'_A/\partial z'(x', L'_{z'}, t') = 0$, and $\partial C'_C/\partial z'(x', L'_{z'}, t') = 0$. Similarly, the vertical walls are impermeable to flow, solute and product, so that $u'(0, z', t') = 0$, $\partial C'_A/\partial x'(0, z', t') = 0$, $\partial C'_C/\partial x'(0, z', t') = 0$; and $u'(L'_{x'}, z', t') = 0$, $\partial C'_A/\partial x'(L'_{x'}, z', t') = 0$, $\partial C'_C/\partial x'(L'_{x'}, z', t') = 0$.

Numerical methods: The coupled nonlinear partial differential equations (1) - (4) subject to relevant boundary conditions were solved numerically using the finite element, partial-differential equation solver Fastflo⁴⁷⁻⁴⁹. The basic solution methods, described in previous publications by the group^{23,27} have been followed. For completeness, we describe these

briefly here. A backward Euler time stepping scheme has been used for time discretisation. The coupled continuity and Darcy's equations were iteratively solved using the augmented Lagrangian method at each time step. Two convergence criteria for velocity \mathbf{v} and pressure p have been satisfied at each time step: (i) the normalized velocity difference between two successive iterations, averaged over all corner nodes $\Sigma |\mathbf{v}_{m,n} - \mathbf{v}_{m,n-1}| / \Sigma |\mathbf{v}_{m,n}| \leq 0.05, \forall m$ for the m -th time step and n -th iteration; (ii) the divergence of velocity satisfies continuity such that $\nabla' \cdot \mathbf{v}' \leq 2 \times 10^{-11}$.

Tests were carried out to ensure that the growth and the evolution of the fingering patterns were independent of mesh and time step resolutions. Six-noded triangular elements with quadratic interpolation were used. The minimum number of nodes required for convergence was found to increase with Da/Ra^2 . The results were found to be independent of time-step for $1.88 \leq t' \leq 3.76$. The Grid Péclet number and Courant number criteria for the minimum required time step was also satisfied, which ensured stability and accuracy of the solutions⁵.

The numerical algorithm was validated against results of Andres and Cardoso²⁷ for zero-density contribution of the product.

C. Methods to find the time for onset of convection

In the linear stability analysis considering the dominant mode of the self-similar diffusion operator, the time for onset of convection, t'_{oc} , corresponds to the time at which the maximum growth rate with respect to the wave number becomes positive. This time denotes the critical time for the onset of instability of the boundary layer.

In the nonlinear simulations, the time for onset of convection t'_{dc} , is obtained by noting the first local minimum in the solute dissolution flux at the interface as a function of time. Beyond this time, convective fingers become noticeable and influence mass transport by convection⁴. This method has been previously used by Hidalgo and Carrera⁵⁰ for an inert system and Andres and Cardoso²¹ for a reactive system.

The linear stability results using the dominant mode (DM) and the quasi-steady state approximation (QSS) are in good agreement. For the inert system, the predicted onset times are consistent with the previously published literature,^{8,10,11} thus validating our methodologies. For the reactive cases, the deviation is even smaller. The general variation of the onset time with reaction strength predicted from nonlinear numerical simulations is in agreement with that obtained from linear stability analysis. For inert systems, Hassanzadeh et al.⁵ reported the time for onset of convection from numerical simulation to be almost an order of magnitude higher than that obtained from linear stability analysis. In the present work, the ratio of time for onset of convection obtained from nonlinear simulations, t_{dc} , to that obtained from linear stability (QSSA and Dominant Mode), t_{oc} , is of this order and is therefore acceptable.

D. Power-averaged mean number of fingers

The power-averaged mean number of fingers,^{27,39} at a given time instant, has been obtained by computing the fast Fourier transform (FFT) of the vertically-averaged solute concentration profile, $\langle C_A'(x', t') \rangle = \int_0^{L_z'} C_A'(x', z', t') dz' / L_z'$. The power-averaged mean number of fingers in the simulation domain is defined as $n(t) = L_x' \sum f_i P_i / \sum P_i$, where f_i are the Fourier modes of the fast Fourier transform $X(f, t)$ and $P_i = |X(f)|^2$ is the corresponding power in the Fourier space.

References

- IPCC. *Special Report on Carbon Dioxide Capture and Storage* (eds Metz, B. et al.), 2005, Cambridge Univ. Press
- H. E. Huppert and J. A. Neufeld, *Annu. Rev. Fluid Mech.*, 2014, **46**, 255–72.
- A. Riaz and Y. Cinar, *J. Petroleum Science and Engg.* 2014, **124**, 367–380.
- H. Emami-Meybodi, H. Hassanzadeh, C. P. Green and J. Ennis-King, *Int. J. Greenhouse Gas Control*, 2015, **40**, 238–266.
- H. Hassanzadeh, M. Pooladi-Darvish and D. W. Keith, *AIChE J.*, 2007, **53**, 1121–1131.
- J. A. Neufeld, M. A. Hesse, A. Riaz, M. A. Hallworth, H. A. Tchelepi and H. E. Huppert, *Geophys. Res. Lett.*, 2010, **37**, L22404.
- D. R. Hewitt, J. A. Neufeld and J. R. Lister, *J. Fluid Mech.*, 2013, **719**, 551–586.
- A. Riaz, M. Hesse, H. A. Tchelepi and F. M. Orr, *J. Fluid Mech.*, 2006, **548**, 87.
- H. Hassanzadeh, M. Pooladi-Darvish, D. W. Keith, *Transp Porous Med.*, 2006, **65**, 193–211.
- D. A. S. Rees, A. Selim and J. P. Ennis King, *Emerging Topics in Heat and Mass Transfer in Porous Media*, Springer, Netherlands, 2008, 85–110.
- M. Chan Kim and C. Kyun Choi, *Phys. Fluids*, 2012, **24**, 044102.
- D. Pritchard, *J. Fluid Mech.*, 2013, **722**, 1–4.
- A. Slim, *J. Fluid Mech.* 2014, **741**, 461–491.
- M. Chan Kim, *Chem. Eng. Sci.*, 2015, **126**, 349–360.
- V. Loodts, L. Rongy, A. De Wit, *Chaos*, 2014, **24**, 043120.
- R. Farajzadeh, B. Meulenbroek, D. Daniel, A. Riaz and J. Bruining, *Comput. Geosci.*, 2013, **17**, 515–527.
- T. J. Kneafsey and K. Pruess, *Transp. Porous Media*, 2010, **82**, 123–139.
- S. Backhaus, K. Turitsyn and R. E. Ecke, *Phys. Rev. Lett.*, 2011, **106**, 104501.
- A. C. Slim, M. M. Bandi, J. C. Miller and L. Mahadevan, *Phys. Fluids*, 2013, **25**, 024101.
- T. F. Faisal, S. Chevalier, Y. Bernabe, R. Juanes and M. Sassi, *Int. J. Heat Mass Transf.*, 2015, **81**, 901–914.
- J. Ennis-King and L. Paterson, *Int. J. Greenhouse Gas Control*, 2007, **1**, 86–93.
- S. S. Cardoso and J. T. Andres, *Nat. Commun.*, 2014, **5**, 5743.
- J. T. Andres and S. S. Cardoso, *Phys. Rev. E*, 2011, **83**, 046312.
- K. Ghesmat, H. Hassanzadeh and J. Abedi, *J. Fluid Mech.*, 2011, **673**, 480–512.
- D. Pritchard and C. N. Richardson, *J. Fluid Mech.*, 2007, **571**, 59–95.
- L. T. Ritchie and D. Pritchard, *J. Fluid Mech.*, 2011, **673**, 286–317.
- J. T. Andres and S. S. Cardoso, *Chaos*, 2012, **22**, 037113.
- M. Chan Kim and C. Kyun Choi, *Phys. Rev. E*, 2014, **90**, 53016.
- T. J. Ward, K. A. Cliffe, O. E. Jensen and H. Power, *J. Fluid Mech.*, 2014, **747**, 316–349.
- T. J. Ward, O. E. Jensen, H. Power and D. S. Riley, *J. Fluid Mech.*, 2014, **760**, 95–126.
- M. A. Budroni, L. A. Riolfo, L. Lemaigre, F. Rossi, M. Rustici and A. De Wit, *J. Phys. Chem. Lett.*, 2014, **5**, 875–881.
- M. Chan Kim, *Chem. Eng. Sci.*, 2015, **134**, 632–647.
- T. J. Ward, O. E. Jensen, H. Power and D. S. Riley, *Phys. Fluids.*, 2015, **27**, 116601.
- V. Loodts, C. Thomas, L. Rongy and A. De Wit, *Phys. Rev. Lett.*, 2014, **113**, 114501.
- C. Wylock, A. Rednikov, B. Haut and P. Colinet, *J. Phys. Chem. B*, 2014, **118**, 11323–11329.
- V. Loodts, L. Rongy and A. De Wit, *Phys. Chem. Chem. Phys.*, 2015, **17**, 29814–29823.
- I. Cherezov and S. S. S. Cardoso, *Phys. Chem. Chem. Phys.*, 2016, **18**, 23727–23736.
- C. Thomas, V. Loodts, L. Rongy and A. De Wit, *Int. J. Greenhouse Gas Control*, 2016, **53**, 230–242.
- A. De Wit, *Physics of Fluids*, 2004, **16**, 163
- Marini, L. *Geochemical Sequestration of Carbon Dioxide* Elsevier, 2007.
- Roscoe Moss Company, *Handbook of groundwater development*, Wiley 1990.
- G. P. D. De Silva, P. G. Ranjith, M. S. A. Perera, *Fuel*, 2015, **155**, 128–143.
- National Chemical Database Service, Royal Society of Chemistry, URL: cds.rsc.org.
- A. C. Lasaga, *Journal of Geophysical Research: solid earth*, 1984, **89**(B6), 4009–4025
- Lecture notes of University of Wisconsin- Green Bay, URL: <https://www.uwgb.edu/dutchs/Petrology/SolnCO3.htm>.
- M. L. Szulczewski, M. A. Hesse, R. Juanes, *J. Fluid Mech.*, 2013, **736**, 287–315.
- CSIRO *Fastflo Tutorial Guide* (CSIRO, Australia, 2000).
- A. N. Campbell, S. S. S. Cardoso, A. N. Hayhurst, *Proceedings of the Royal Society of London A: Mathematical, Physical and Engineering Sciences*, 2005, **461**, 1999–2020.
- A. N. Campbell, S. S. S. Cardoso, A. N. Hayhurst, *Chemical Engineering Science*, 2005, **60**, 5705–5717.
- J. J. Hidalgo and J. Carrera, *J. Fluid Mech.*, 2009, **640**, 441